




# Multiscale topology optimization for non-uniform microstructures with hybrid cellular automata

Jiao Jia<sup>1,2</sup> · Daicong Da<sup>3</sup> · Cha-Liang Loh<sup>4</sup> · Haibin Zhao<sup>4</sup> · Sha Yin<sup>1,2</sup> · Jun Xu<sup>1,2</sup> 

Received: 3 August 2019 / Revised: 29 January 2020 / Accepted: 10 February 2020  
© Springer-Verlag GmbH Germany, part of Springer Nature 2020

## Abstract

Based on hybrid cellular automata (HCA), we present a two-scale optimization model for heterogeneous structures with non-uniform porous cells at the microscopic scale. The method uses the  $K$ -means clustering algorithm to achieve locally nonperiodicity through easily obtained elemental strain energy. This energy is used again for a two-scale topological optimization procedure without sensitivity analysis, avoiding drastically the computational complexity. Both the experimental tests and numerical results illustrate a significant increase in the resulting structural stiffness with locally nonperiodicity, as compared to using uniform periodic cells. The effects of parameters such as clustering number and adopted method versus classical Optimality Criteria (OC) are discussed. Finally, the proposed methodology is extended to 3D two-scale heterogeneous structure design.

**Keywords** Concurrent optimization · Hybrid cellular automata · Clustering algorithm · Non-uniform microstructure

## 1 Introduction

Lightweight structures are the long-time pursuit of human society for more sustainable lives (Schaedler et al. 2011; Wang et al. 2016; Yin et al. 2017). With the development of understanding of material structure-property, designing materials from a variety of length scales, from nano-scale (Baughman et al. 2002), microscale (Evans et al. 2001; Xu et al. 2018; Xu et al. 2019) to macro-scale (Xie et al. 2012) and multi-scales (Yao et al. 2011; Zhang et al. 2019), is regarded as one of the most promising methodologies for improving and

optimization of mechanical performance of structures (Lakes 1993; Zhang et al. 2011).

One of the key problems for material design is the material distribution over the various length scales. Generally, elegant and smart topology optimization methodology is needed for integration macro structure performance with micromaterial properties. Pioneering researchers such as Rodrigues et al. (Rodrigues et al. 2002) firstly achieved a hierarchical topology optimization technique with material distribution varying from point to point. Later, this model was extended to a 3D problem (Coelho et al. 2008). This approach can maximize the structural optimization capacity in theory. However, the major disadvantage of this methodology costs massive computational resources and results in the poor manufacturability. To satisfy the constraints of manufacturing, under the framework of solid isotropic material with penalization (SIMP), Liu et al. (Liu et al. 2008) proposed a popular concurrent optimization model with a uniform microstructure. Lining with this idea, concurrent optimization with diverse physical problems is widely discussed, e.g., dynamic problem (Niu et al. 2009), thermoelastic problem (Deng et al. 2013), and acoustic problem (Liang and Du 2019). Besides the SIMP method, bidirectional evolutionary structural optimization method with black-and-white material distributions also contributed intensively in two-scale optimization (Da 2019; Xu et al. 2016; Xu and Xie 2015; Yan et al. 2014; Yan et al. 2015). It is obvious that consideration of point-to-point material distribution in microstructure level is usually

---

Responsible Editor: Raphael Haftka

✉ Sha Yin  
junxu@buaa.edu.cn

✉ Jun Xu  
shayin@buaa.edu.cn

<sup>1</sup> Vehicle Energy & Safety Laboratory (VESL), Beihang University, Beijing 100191, China

<sup>2</sup> Department of Automotive Engineering, School of Transportation Science and Engineering, Beihang University, Beijing 100191, China

<sup>3</sup> Laboratoire Modélisation et Simulation Multi Echelle MSME, Université Paris-Est, UMR CNRS 8208, 5 bd Descartes, 77454 Mame-la-Vallée, France

<sup>4</sup> Changshu Automotive Trim Co., Ltd., Changshu 215500, China

redundant and low-efficiency, homogeneous material design is always far from optimal performance. By carefully observing the structure in nature, e.g., animal bone and nacre shell, one may observe that the structure can be generally divided into several regions and the material topologies in the same region are alike which provides us a new route for achieving good manufacturability while obtaining certain material distribution for good mechanical properties with limited design elements. By bearing such idea in mind, Zhang and Sun (Zhang and Sun 2006) investigated the scale effect when cellular materials present the graded distributions on the macro-scale. In the research of Sivapuram et al. (Sivapuram et al. 2016), the non-uniform microstructures with porous present worse stiffness performance than the solid structures with the same material dosages. Based on a multilevel finite element approach (Feyel and Chaboche 2000), a non-uniform nonlinear multiscale computing scheme is established by Xia and Breitkopf (Xia and Breitkopf 2014). In considering the manufacturability, Wang et al. (2018) recently developed an approach to optimize the structure filled with parameterizable non-uniform lattice microstructures. Focusing on comparing the superiority of multipatch structure with macro-scale structure, a series of work with the level set method were detailed described in recent research work (Gao et al. 2019a; Gao et al. 2019b; Li et al. 2018).

As an effective nongradient optimization approach, hybrid cellular automata (HCA) is inspired by the biological process of bone remodeling and obeys a full-stressed principal. In HCA methodology, the design domain is discretized by cellular automata (CA) cells. By using the finite element method (FEM) to evaluate the strain energy density, Tovar et al. (Tovar et al. 2006) developed the local control rules to improve the model stability and numerical efficiency in topology optimization. Generally speaking, HCA has advantages in nonlinear problems, e.g., crashworthiness topology optimization (Patel et al. 2009), and more recently, HCA has been extended to be applied in material design (Da et al. 2017).

This work aims to develop and extend the HCA methodology to concurrent design with consideration of non-uniform microstructures. With the help of an energy-based homogenized approach (Jie et al. 2018; Xia and Breitkopf 2015), the elemental strain energy (ESE) on macro and microscales is deduced. In terms of the clustering algorithm, the macro ESE is divided into several levels to limit the categories of microstructures. Moreover, the design variable update rules with mass constraints are respectively established according to the deduced ESE. The remainder of this paper is organized as follows. The clustering concurrent optimization model with HCA is described in detail in Section 2. In Section 3, a quasi-static test is conducted to demonstrate the effectiveness of the proposed method. In Section 4, the governing factors of the optimization results and model adaption in the 3D design are discussed through several numerical examples. Finally, concluding remarks are given in Section 5.

## 2 Optimization methodology

As illustrated in Fig. 1, the macrostructure contains several disparate patterned microstructures and each of them is periodically distributed within different regions according to load-bearing capacity. In HCA methodology, the design domain is discretized by CA cells and the state of each CA cell is decided by design variable and field variable together. On the macro scale, the design domain is discretized by  $M$  CA cells and each macro CA cell corresponds to a cellular structure on micro-scale. Take the elemental relative density  $P_m$  ( $m = 1, 2, \dots, M$ ) and  $r_{kn}$  ( $k = 1, 2, \dots, K, n = 1, 2, \dots, N$ ) as the macro and microdesign variables, respectively where  $K$  stands for the total types of microstructures and  $N$  stands for the numbers of CA cells within a microstructure. Both  $P_m$  and  $r_{kn}$  vary between  $[\delta, 1]$  to represent the cell is solid or void where  $\delta$  is set to be 0.001 to avoid numerical singularity in the optimization process. The selection of the field variables depends on the specific physical problem. Different from the conventional CA method, the HCA utilizes the FEM to obtain the field variable. If the structure has higher stiffness, the lower strain energy it stores. In a domain discretized by FEM, the strain energy can be expressed

as  $C = \sum_{m=1}^M C_m$ , where  $C_m$  is the ESE. Therefore, the ESE is

the local indicator to evaluate the structural stiffness and is naturally be chosen as the field variable in stiffness optimization with HCA. It is noted that the CA cells are coincident with the finite element (FE) meshes in this research. Without gradient information, the quantity of material added or removed in each iteration is locally manipulated by different levels between actual ESE and target value.

Based on the above description, the two-scale optimization model considering non-uniform microstructures can be formulated as

$$\begin{cases} \text{find } \{P_m, r_{kn}\} \\ \min C = \frac{1}{2} \sum_{m=1}^M \mathbf{U}_m^T \mathbf{K}_m(P_m, r_{kn}) \mathbf{U}_m & (1.1) \\ \text{s. t. } \mathbf{K}\mathbf{U} = \mathbf{F} & (1.2) \\ \sum_{m=1}^M P_m V_m / V_0^{\text{mac}} = V^{\text{mac}} & (1.3) \\ \sum_{n=1}^N r_{kn} V_{kn} / V_{k_0}^{\text{mic}} = V_k^{\text{mic}} & (1.4) \end{cases}$$

where  $C$  denotes the structural compliance;  $\mathbf{U}_m$  and  $\mathbf{K}_m$  are the macro-elemental stiffness matrix and displacement vector. In Eq. (1.2),  $\mathbf{K}$ ,  $\mathbf{U}$ , and  $\mathbf{F}$  represent the global stiffness matrix, displacement vector, and load vector, respectively. Equations (1.3) and (1.4) respectively restrict the dosages of materials on macro and microscales to be equal to  $V^{\text{mac}}$  and  $V_k^{\text{mic}}$ , where  $V_m$  and  $V_{kn}$  are the macro and micro-elemental volume, respectively.  $V_0^{\text{mac}}$  and  $V_{k_0}^{\text{mic}}$  are defined as the macro and microvolumes of solid design.

According to the description in Eq. (1), the two-scale optimization with HCA includes the following three key steps, i.e., (step 1) deduction of ESE on two scales; (step 2) material

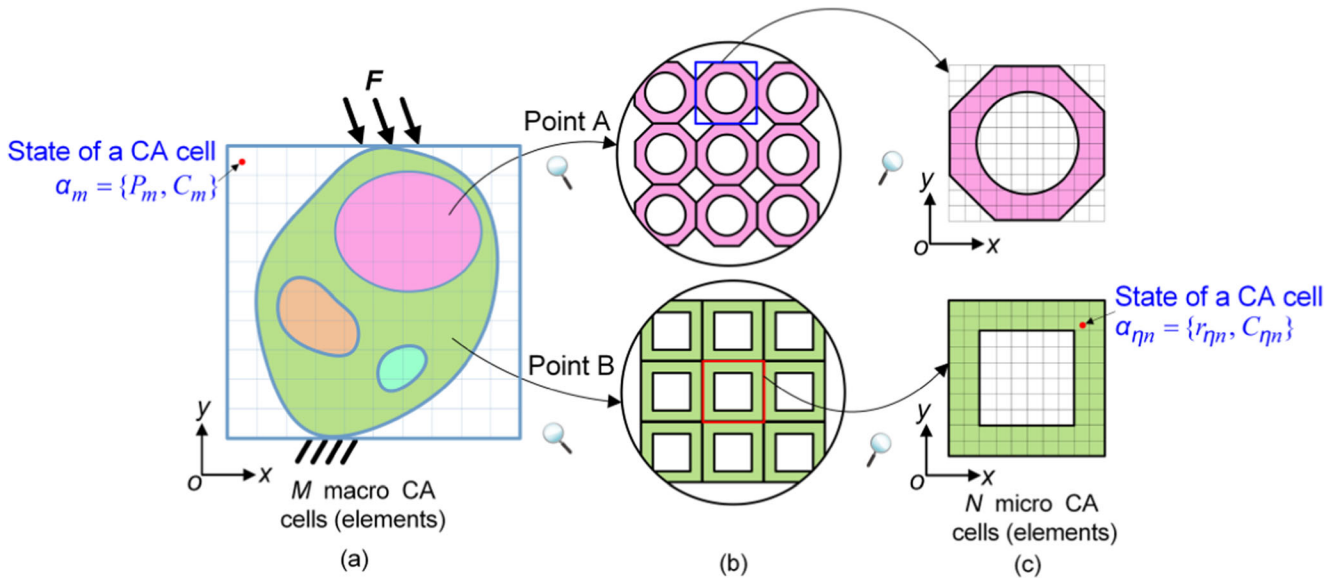


Fig. 1 Two-scale clustering optimization with HCA: **a** macrostructure, **b** non-uniform materials, and **c** unit cells

clustering distributions on macro-scale; and (step 3) update rules of design variables and convergence condition.

### 2.1 Deduction of ESE on two scales

On the microscale, the SIMP interpolation is adopted to characterize the modulus at a cell/element in the group  $k$  as

$$E_{kn} = E_{\min} + (r_{kn})^q (E_0 - E_{\min}) \quad (2)$$

where  $E_0$  is Young’s modulus of base material and  $E_{\min}$  is a

very small value to avoid the possible singularity. The value of the penalty exponent  $q$  is set to be 4 to guarantee a black-and-white material distribution (Da et al. 2017).

The relationship between macro and microscales depends on the material effective elastic tensor  $D^H$ . In the energy-based homogenization approach, the effective elastic tensor of the group  $k$  can be approximated in terms of element mutual energies (Jie et al. 2018; Xia and Breitkopf 2015).

$$D_{ijst}^H(k) = \frac{1}{|Y|} \sum_{n=1}^N Q_{ijst}^{kn} = \frac{1}{|Y|} \sum_{n=1}^N \left( \mathbf{u}_{ij}^{kn} \right)^T \mathbf{k}_{kn} \mathbf{u}_{st}^{kn} \quad (3)$$

Fig. 2 2D and 3D CA neighborhood layouts: **a** 2D empty  $ne = 0$ , **b** 2D Von Neumann  $ne = 4$ , **c** 3D empty  $ne = 0$ , **d** 3D Von Neumann  $ne = 6$ , and **e** 3D radial  $ne = 18$

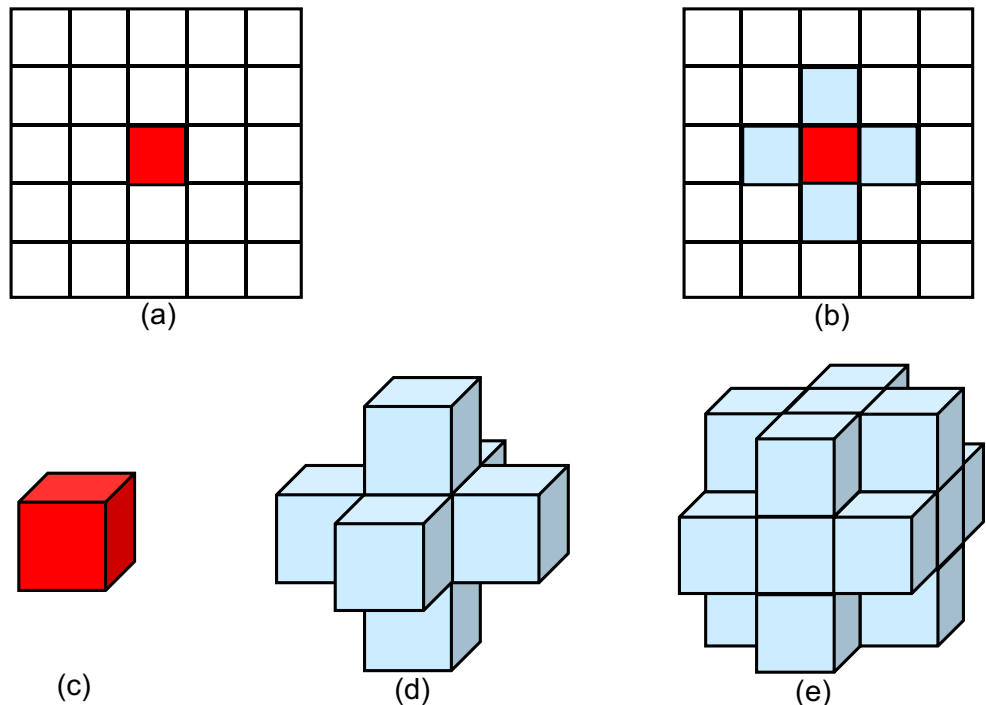
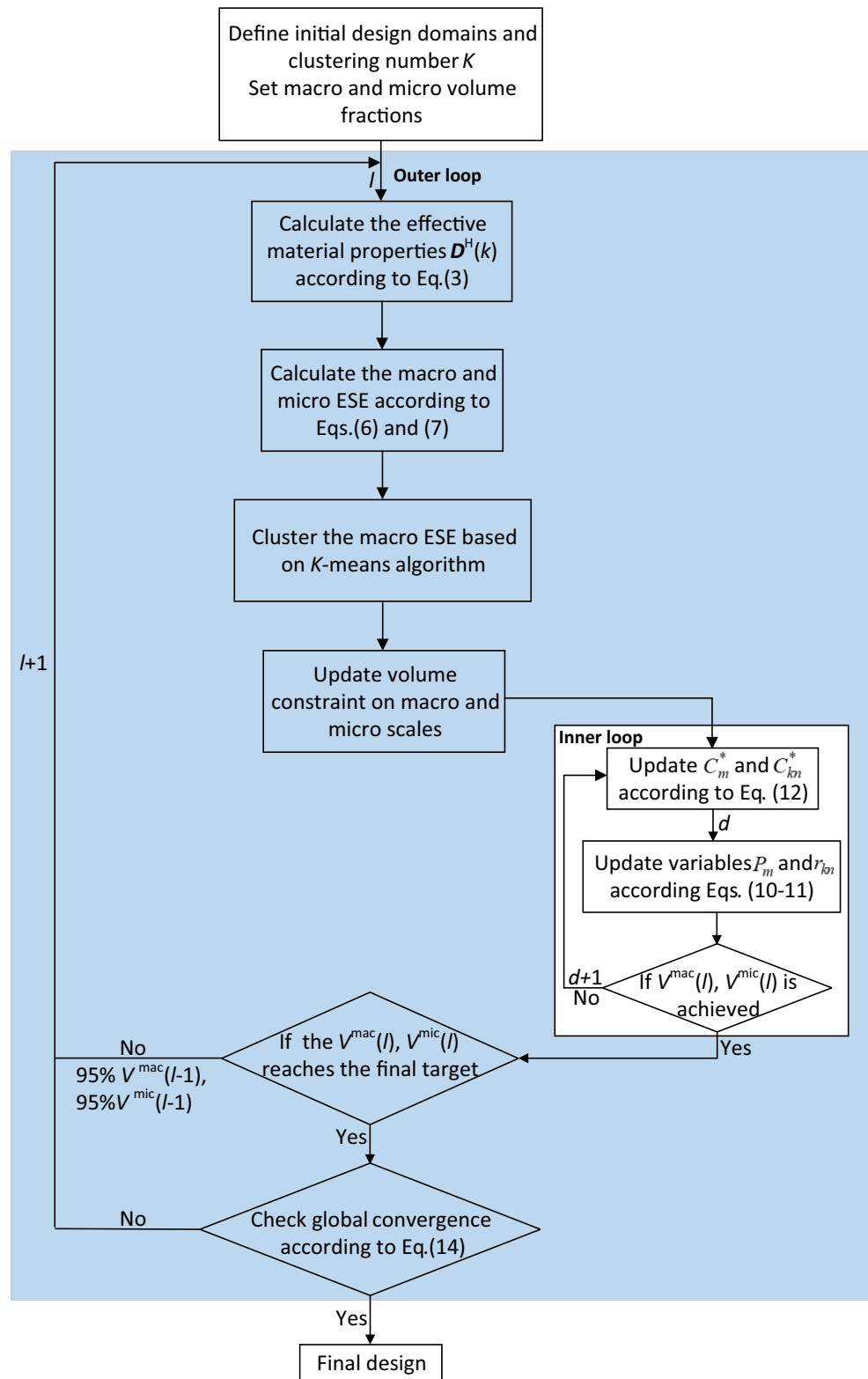


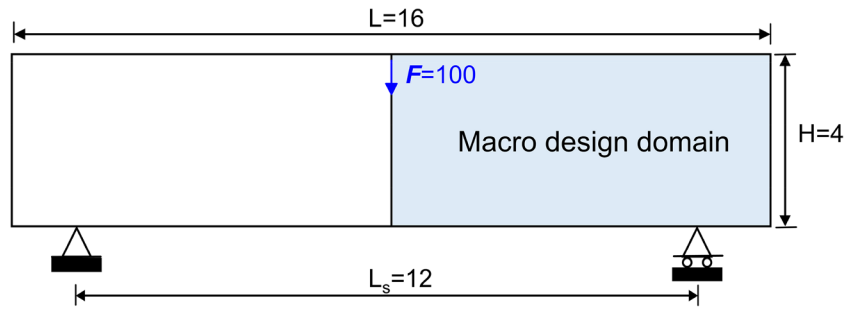
**Fig. 3** Flow chart of achievement of clustering design with HCA



where  $|Y|$  is the area in 2D or the volume in 3D of microstructure.  $Q_{ijst}^{kn}$  denotes the element mutual energies in  $k$ th the microstructure. As to 2D case,  $i, j, s, t = 1, 2$  and  $i, j, s, t = 1, 2, 3$  in 3D case.  $u^{kn}$  stands for the induced element displacements

which can be obtained by the equilibrium equation of force-displacement (Jie et al. 2018; Xia and Breitkopf 2015). Micro-elementary stiffness  $k_{kn}$  can be obtained through the integration on elemental volume  $V_{kn}$ , as  $E_{kn} \int_{V_{kn}} \mathbf{b}^T \mathbf{D}_0 \mathbf{b} dV_{kn}$ , where  $\mathbf{b}$

Fig. 4 Schematic 2D design domain and boundary conditions



is the microstrain-displacement matrix,  $\mathbf{D}_0$  is the elasticity matrix without multiplying Young’s modulus. If the macrostructure is composed of  $K$  types of microstructures, the homogenization method will be correspondingly called  $K$  times to evaluate the performance of different microstructures.

On the macro scale, the effective elasticity matrix of element  $m$ ,  $\mathbf{D}_m^{MA}$ , filled with microstructure  $k$  can be interpolated by the porous anisotropic material with penalization model (Liu et al. 2008) as

$$\mathbf{D}_m^{MA}(k) = P_m^p \mathbf{D}^H(k) \tag{4}$$

$p$  is the macro penalization factor with the typical value of 3.

Furthermore, the global stiffness matrix  $\mathbf{K}$  can be written as the assembling of elemental stiffness matrix  $\mathbf{K}_m$

$$\mathbf{K} = \sum_{m=1}^M \mathbf{K}_m = \sum_{m=1}^M \int_{V_m} \mathbf{B}^T \mathbf{D}_m^{MA}(k) \mathbf{B} dV_m \tag{5}$$

where  $\mathbf{B}$  is the macro strain-displacement matrix. When the element  $m$  is occupied by the microstructure  $k$ , the elemental stiffness matrix should be expressed by the integration of corresponding material properties.

With applying the load and boundary conditions, we can have the macro ESE through the FE analysis, as

$$C_m = \frac{1}{2} \mathbf{U}_m^T \mathbf{K}_m \mathbf{U}_m \tag{6}$$

Correspondingly, the entire structural strain energy assigned to element  $n$  in microstructure  $k$  can be deduced as

$$C_{kn} = \frac{1}{2} \sum_{m=1}^M P_m^p \mathbf{U}_m^T \int_{V_m} \mathbf{B}^T \frac{1}{|Y|} \mathbf{Q}^{kn} \mathbf{B} dV_m \mathbf{U}_m \tag{7}$$

In the CA paradigm, the final field variable is mutually decided by the neighborhood CA cells. Take average ESE on macro-scale,  $\bar{C}_m$ , as an illustration

$$\bar{C}_m = \frac{C_m + \sum_{e=1}^{ne} C_e}{ne + 1} \tag{8}$$

where  $C_e$  corresponds to the strain energy of a neighboring cell/element and  $ne$  is the number of neighbors defined in the CA paradigm. As shown in Fig. 2 b and d, the von Neumann layout, including 4 neighbors in 2D and 6 neighbors in 3D, is respectively employed in 2D design and 3D microdesign in this work. For obtaining wider structural members, a radial 18-neighbors layout (Fig. 2e) is adopted in 3D macro optimization. Actually, the use of average strain energy instead of an actual value can be viewed as a filtering technique that prevents the checkerboard and mesh dependency phenomena in the optimization process.

### 2.2 Material clustering distribution on macro-scale

To achieve the non-uniform distributions of materials on the macro-scale, the clustering algorithm used to categorize data into groups with similar characteristics is employed to cluster the macro ESE. Note that the  $K$ -means ( $K$  stands for numbers

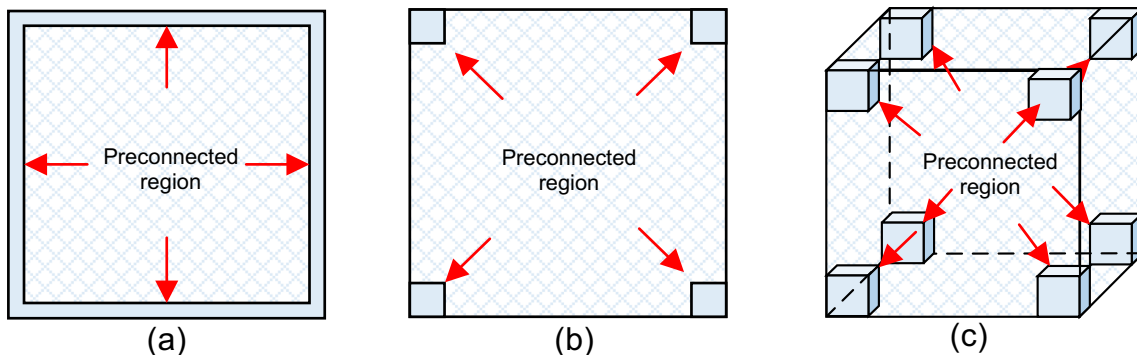


Fig. 5 Kinematical connectivity between nonperiodic microstructures in 2D and 3D

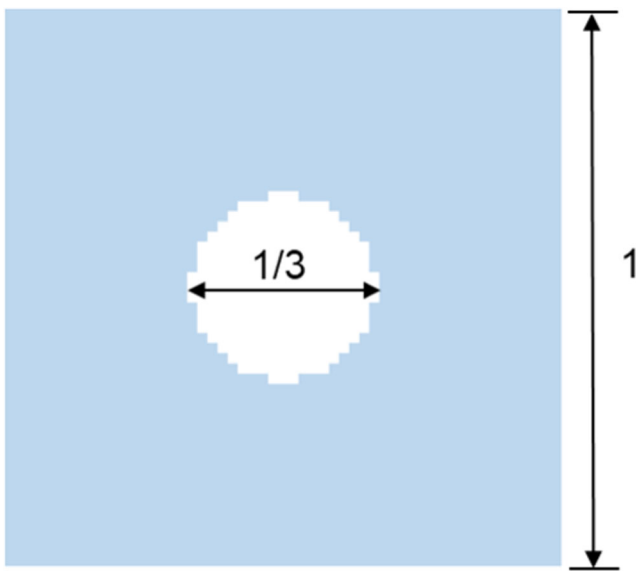


Fig. 6 Initial design

of clusters) algorithm (Tan et al. 2006) is adopted in this work, and other clustering methods can work similarly as well. The detailed process of clustering ESE can be implemented after the macro FE analysis and summarized as follows.

Step 1: Select  $K$  ESE as the initial cluster centers, and calculate the norm distance between ESE and each cluster center as

$$D_{km} = \sqrt{(C_m - C_k)^2} \tag{9}$$

Step 2: If  $C_m$  is closest to the cluster center  $C_k$  among all cluster centers, the element  $m$  is categorized into the group  $k$ ;

Step 3: Take the average strain energy of each group as the new cluster center until the cluster center keeps constant.

Fig. 7 The optimized structures for 3D printing: **a** non-uniform microstructures, and **b** uniform microstructure

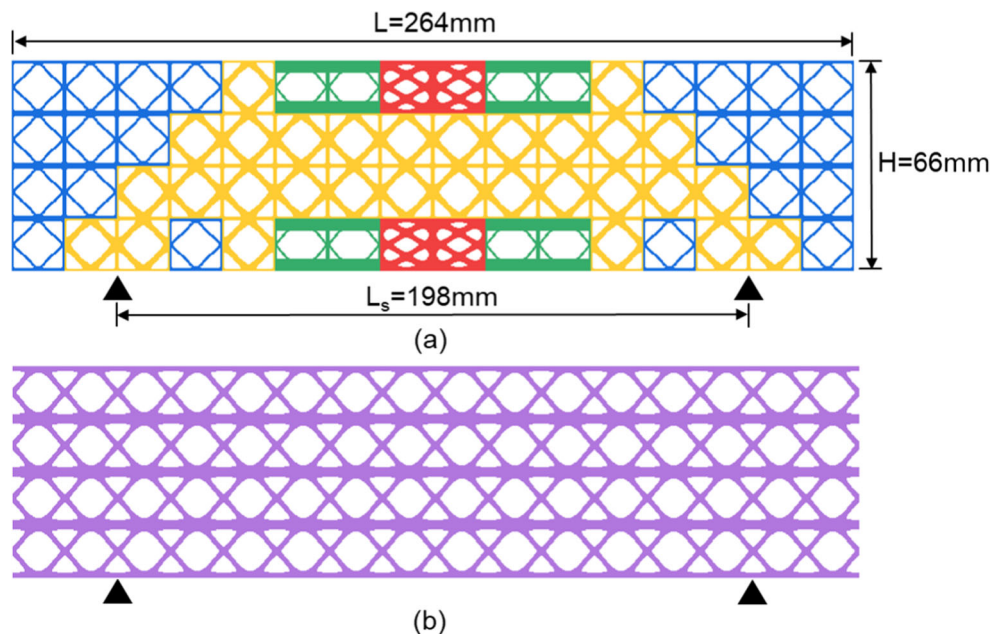


Table 1 The properties of the resin for 3D printing

Parameters	Value
Tensile modulus	2370–2650 MPa
Tensile strength	35 MPa
Flexural modulus	2178–2222 MPa
Flexural strength	67 MPa
Elongation at break	6–9%
Poisson’s ratio	0.41
Density	1.16 g/cm <sup>3</sup>

### 2.3 Updating rules

For minimizing the deviation between the target and the actual value of ESE, the local design rule using the concept of proportional control theory is adopted. For simplicity, macro design variable  $P_m$  is taken as an example to demonstrate the updating strategy for microdesign variables. It can be updated as

$$P_m(l + 1) = P_m(l) + \Delta P_m(l) \tag{10}$$

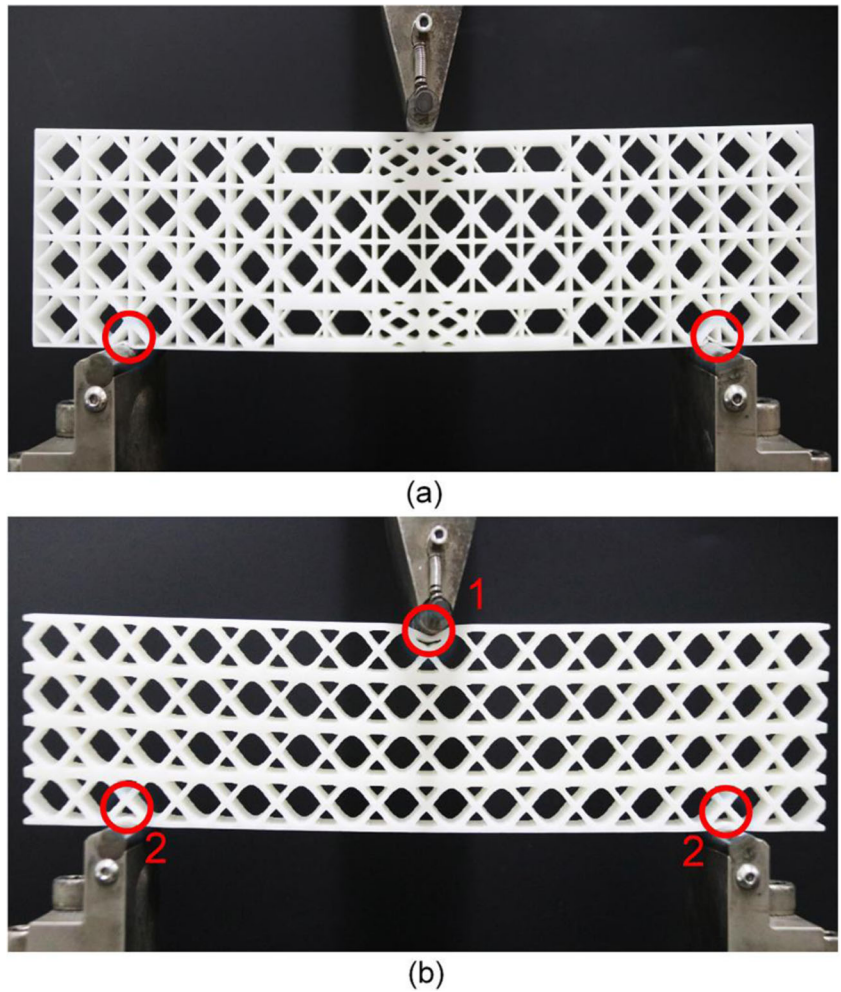
where  $l$  stands for the current iteration. The change in design variable  $\Delta P_m(l)$  can be stated as

$$\Delta P_m(l) = c_p \times \left( \bar{C}_m / C_m^* - 1 \right) \tag{11}$$

where  $c_p$  is the proportional gain to control the amplitude change of the design variables. The suggested range of  $c_p$  is 0.15~0.5 which is determined by the numerical examples.  $C_m^*$  is the local macro strain energy target.

It is observed that with the setpoint value  $C_m^*$  increasing, the volume of the resulting topology decreases and vice versa,

**Fig. 8** The quasi-static tests of optimized structures: **a** non-uniform microstructures, and **b** uniform microstructure



serving as the foundation of volume constraint. To achieve the final volume, the elements are evolutionarily removed for satisfying the changing volume target during each design iteration. Moreover, a secondary inner iteration is used in  $l$ th the design step with updating  $C_m^*$  iteratively until the volume constraint is satisfied which can be written as

$$C_m^*(d + 1) = C_m^*(d) \left( \frac{V_f^{\text{mac}}(d)}{V^{\text{mac}}(l)} \right) \tag{12}$$

where  $d$  is the iterator in the sub-loop.  $V_f^{\text{mac}}$  is the material volume fraction in the macro design domain.  $V^{\text{mac}}(l)$  is the volume fraction target in single design iteration, which is set as 95% of  $V^{\text{mac}}(l - 1)$ .

In the optimization, the volume fraction constraints for macro and microscales should be assigned according to the specific requirements. In this research, the volume fraction constraints of non-uniform microstructures satisfy the relationship as

$$V_k^{\text{mic}} = V_{\text{min}}^{\text{mic}} + (V_{\text{max}}^{\text{mic}} - V_{\text{min}}^{\text{mic}}) \left[ \frac{(K - K_k)}{(K - 1)} \right]^\zeta \tag{13}$$

where  $V_{\text{max}}^{\text{mic}}$  and  $V_{\text{min}}^{\text{mic}}$  restrict the variation range of microvolume fractions.  $K_k$  is the microstructure index from  $[1, \dots, K]$ . Specifically, when a parameter  $\zeta = 1$ , the microvolume fractions will change linearly.

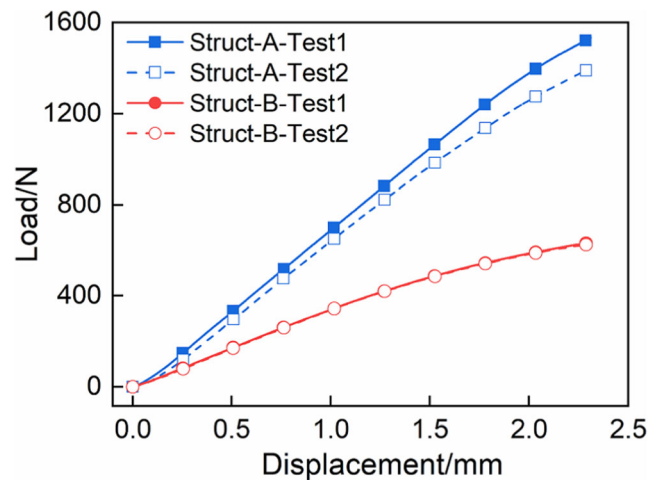


**Fig. 9** The experimental force-displacement curve of optimized structures

**Table 2** Macromaterial distributions and optimized microstructures with different  $K$

Types of microstructures	Macro material distributions	Non-uniform microstructures	Equivalent micro volume fraction(%)	Uniform microstructure with equivalent volume
$K=2$			30.05	
$K=3$			34.46	
$K=4$			36.88	
$K=5$			42.77	
$K=6$			42.97	

The optimization will stop when no further change in macro and microvolumes at the same time (Tovar et al. 2006). Such criteria can be expressed as

$$\frac{|\Delta V(l)| + |\Delta V(l-1)|}{2V_0} \leq \varepsilon \tag{14}$$

where  $V_0$  stands for the volume of solid design on macro or microscale.  $\Delta V(l) = V(l) - V(l - 1)$ , where  $V(l)$  and  $V(l - 1)$  include the macro and microvolumes in  $l$ th and  $(l - 1)$ th iteration steps. Based on trial testing, the convergence tolerance  $\varepsilon$  is set as 0.01% in this work for clearer topologies.

According to the description above, the key steps for the achievement of clustering design with HCA are given in Fig. 3.

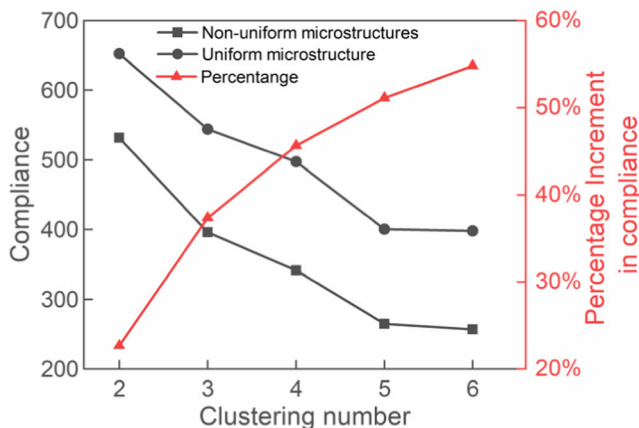


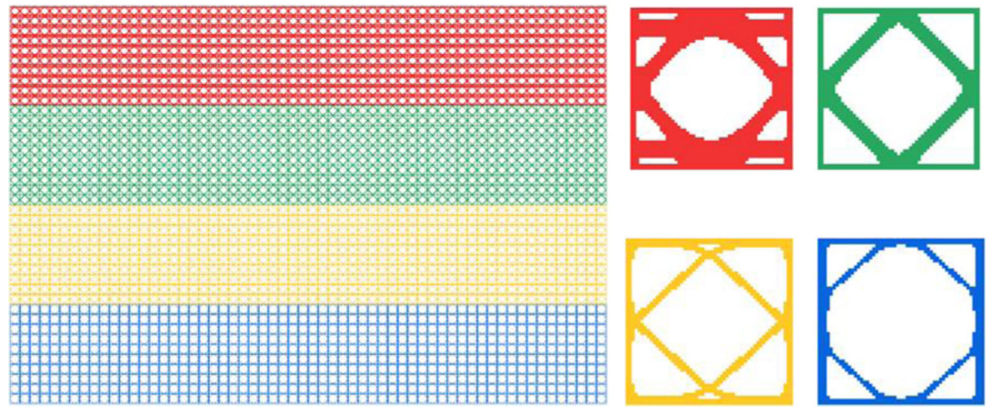
**Fig. 10** Comparisons between non-uniform and uniform microstructures

### 3 Experimental validation

By means of the three-point flexural experiment, the performance improvement of multi microstructures and the capability of the proposed methodology for optimizing the non-uniform microstructures are validated. As illustrated in Fig. 4, a 2D beam under a concentrated force located at the center of the top edge is optimized for experimental validation. For the sake of discussions, the structural sizes, material properties, and external loads are all dimensionless for numerical design. The material parameters are assumed as Young’s modulus is  $E = 2000$ , and Poisson’s ratio  $\nu = 0.41$ . The load magnitude is supposed as  $F = 100$ . For a simple comparison, the 2D beam optimization has no macrostructure design, that is  $P_m \equiv 1$ . Due to symmetry, only the right-hand half the beam, composed of 4 and 1 microstructures respectively, is considered in the optimization process. The 3D printing technique is adopted to fabricate the optimized structures in consideration of its superior ability to produce complex structures. As we all know, the unit cell should be infinitesimally small compared with the macrostructures according to the homogenization theory. However, because of the limits of the 3D printer and experiment conditions, the macro design domain has to be divided into  $8 \times 4$  elements with a size of 1. The microstructures are discretized into  $55 \times 55$  4 node quadrilateral plane stress elements with the dimensionless size of 1. Moreover, the displacements are confined at the locations for ensuring the support span length is less than 200 mm. For ensuring the continuity, a number of nondesign elements are preset as kinematically connective



**Fig. 11** Gradient structure composed of four microstructures



constraints between the adjacent microstructures (Zhou and Li 2008). The connectors in Fig. 5 are adopted in the design of the experiment. As illustrated in Fig. 6, all the microstructures start from an initial guess design which assigns a circular void region in the center of the microdesign domain. In the design of 4 microstructures, the microvolume fraction constraints linearly vary between [30%, 70%], i.e.,  $V_1^{\text{mic}} = 30\%$ ,  $V_2^{\text{mic}} = 43.33\%$ ,

$V_3^{\text{mic}} = 56.67\%$ , and  $V_4^{\text{mic}} = 70\%$ . To guarantee the same material dosages, the volume fraction constraint in uniform microstructure is set as  $V_1^{\text{mic}} = 42.08\%$ . The post-processing step given in (Sigmund and Maute 2013) is used to eliminating the intermediate variables completely in the numerical results. In the results of clustering optimization, red, green, yellow, and blue represent the dosages of material on microscale from large

**Fig. 12** Resulting macrostructures and its microstructures versus disparate  $V^{\text{mac}}$

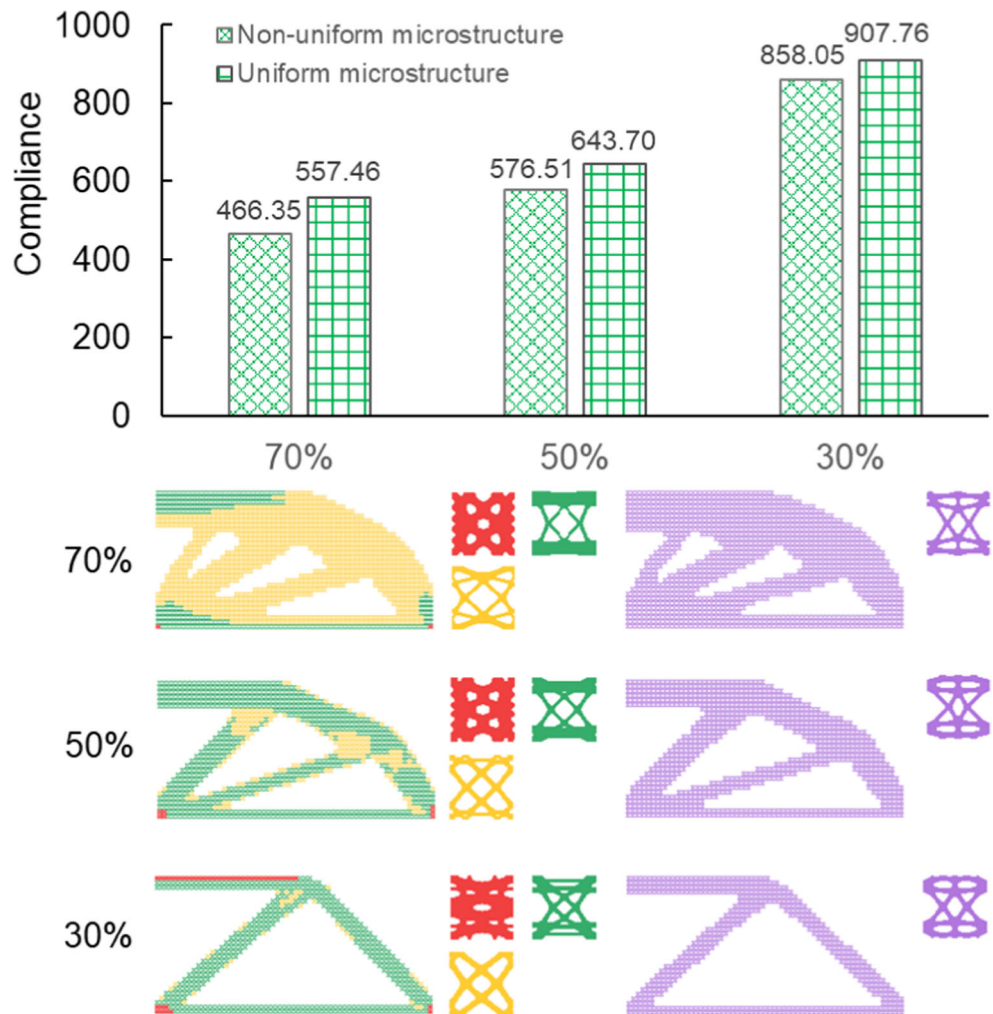


**Table 3** Percentages of microstructures with decreasing of  $V^{mac}$

$V^{mac}$ (%)	Microstructure 1 (%)	Microstructure 2 (%)	Microstructure 3 (%)
70	0.16	18.17	81.67
50	0.78	77.09	22.14
30	7.42	85.71	6.86

to small. Note that the same color is used to reflect the corresponding distributed locations on the macro-scale.

The resulting beams with 4 microstructures (Struct-A) and uniform microstructure (Struct-B) are illustrated in Fig. 7. The final compliance is  $C = 174.46$  and  $261.56$ , respectively. In Fig. 7 a, the regions of material distribution reasonably exhibit the contributions of different parts responding to the external load. The numbers of red microstructure are 4, which are located at the middle of the top and bottom edges. Besides the red microstructures, the green microstructures are also the primary bearing-load materials and distributed beside the red microstructures. The yellow microstructures mainly act as a role of load transmitting. Besides, the yellow microstructures are observed to be distributed within the constraints applying zones. Due to almost no load-bearing capacity, the blue microstructures just fill in the rest of the regions.

The optimized results are fabricated by the UnionTech 3D printer with resin material whose specific performance has been provided in Table 1. With the size of the unit cell as  $16.5 \text{ mm} \times 16.5 \text{ mm}$ , the dimensions of the beam are length  $L = 264 \text{ mm}$ , support span length  $L_s = 198 \text{ mm}$ , height  $H = 66 \text{ mm}$ , and width  $B = 13 \text{ mm}$ . The final mass of the beams varies between  $111.39$  and  $111.55 \text{ g}$ . The quasi-static tests were performed with INSTRON 2345 and the loading rate is set as  $0.5 \text{ mm/min}$ . The experiment for the same structure was repeated twice, called as test 1 and 2 respectively.

From Fig. 8 a, it is known that since the microstructures with the force directly applied were strengthened, the regions of the most prone to deformations in Struct-A were located at

the positions where the displacements were confined (red circled regions). Different from Struct-A, the deformation of the Struct-B firstly initiated at the point of load applied (red circled region with 1 in Fig. 8b). Then, the deformation was triggered at the positions where the displacements were restricted (red circled regions with 2 in Fig. 8b).

As illustrated in Fig. 9, the slope of the force-displacement curve of Struct-A is obviously larger than the value of Struct-B, which generally reflects that the Struct-A has superior in stiffness than the Struct-B. As to Struct-A, the stiffness difference between test 1 and 2 is caused by the random factors in manufacturing. The average slopes of curves in Fig. 9 can be calculated as  $669.40 \text{ N/mm}$  and  $284.15 \text{ N/mm}$ , respectively. According to the test standard (ASTMInternational 2015), the flexural secant modulus of elasticity can be evaluated by  $E_f^{secant} = \frac{L_s^2 w}{4HB^3}$ , where  $w$  is the slope of the force-displacement curve. For the same  $L_s$ ,  $H$ , and  $B$ , the final flexural secant modulus of Struct-A is 2.36 of Struct-B. Due to the stiffness that can be evaluated by the reciprocal of compliance, the ratio of  $1/C$  between Struct-A and Struct-B is equivalent to the ratio of slopes between them. With the compliance provided, the numerical flexural secant modulus of the Struct-A is 1.50 of the Struct-B. For size effect and certain simplicity of the model, the numerical results cannot match the experimental results well. Despite the differences in values, both the numerical and experimental results reveal that the structure composed of a variety of microstructures has better stiffness performance than the structure with uniform microstructure. Furthermore, the effectiveness of the proposed method in designing the clustering structure is validated as well.

### 4 Numerical discussions

By means of several numerical examples, the effects of parameters, e.g., clustering number  $K$ , macro volume constraint  $V^{mac}$ , and model adaption, are detailed discussed in this

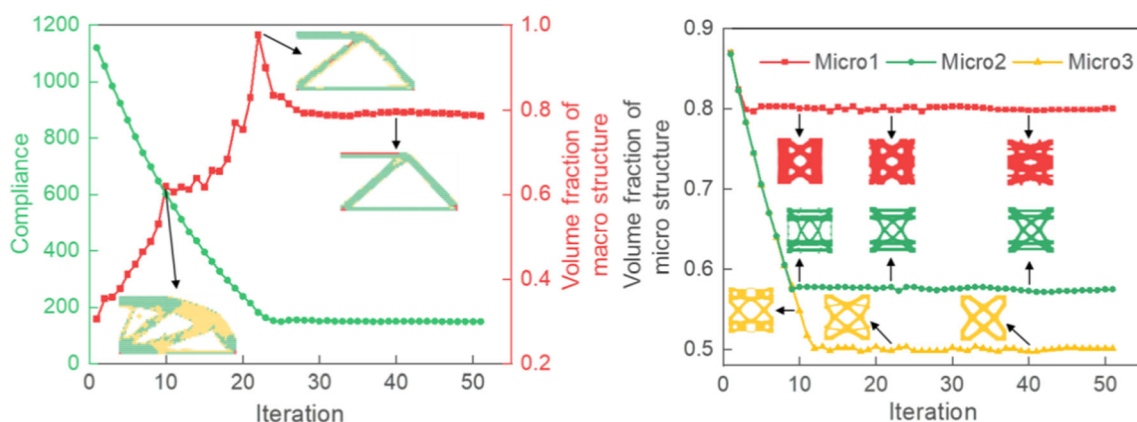


**Fig. 13** Iterations of compliance, macro and microvolume fractions with  $V^{mac} = 30\%$

section. The connectors in Fig. 5 a–c are sequentially accepted in the 2D and 3D examples. The macro- and micro-2D element sizes and the material parameters are consistent with the values used in the experimental design except the Poisson’s ratio  $\nu = 0.3$ . In the 3D case, the microstructures are discretized into  $30 \times 30 \times 30$  8 node brick elements. The magnitude of the load keeps  $F = 100$ . Red, green, orange, blue, magenta, and cyan indicate a gradual decrease in the dosages of material on microscale. Without a redundant explanation, the final results are all be post-processed to eliminate the intermediate variables.

### 4.1 2D examples

Minor different with the design domain in Fig. 4, the geometric parameters are changed as length  $L = 120$ , height  $H = 40$  in Example I, and  $H = 30$  in Example II, respectively. The displacements restrictions are moved to the left and right bottom corners, respectively. In the first example, the load is applied to the same place in Fig. 4, while it moves to the center of the bottom edge in the second example.

**Example I** The influences of  $K$  are investigated with changing  $K$  from 2 to 6. With  $\zeta = 1$ , the ranges of microvolume fractions are the same as the experimental design. Still, without the macro design, the optimized topologies are illustrated in Table 2. For comparison, with the same material consuming, the optimized uniform microstructures corresponding to different  $K$  are orderly exhibited in Table 2 as well.

From Table 2, it is known that, altering  $K$  from 2 to 6, the numbers of red microstructure always keep 3. One is located at the point of force applied and the other two are located in the right corner with implementing the boundary conditions. The contributions of different parts are evolutionally revealed with increased  $K$ , i.e., around the vicinity of force, constraint applying zones, and the left bottom edge, the different types of

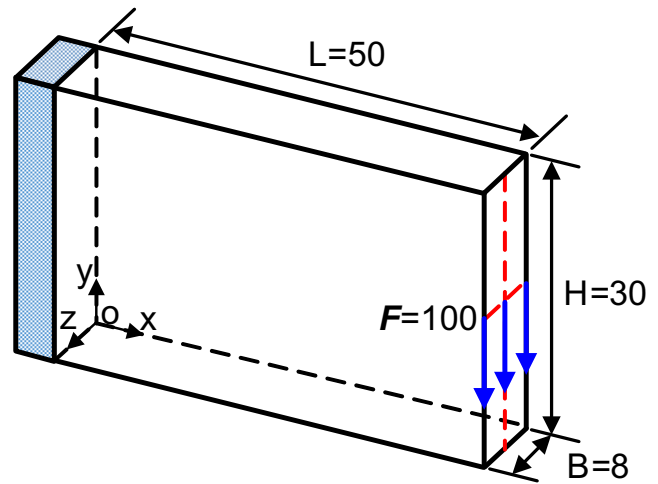


Fig.14 A 3D cantilever beam structure

microstructures distribute from inside to outside like a ring according to their bearing capacity. Besides, the microstructures barely without the load capacity are mainly distributed in the middle and right upper corner regions of the macrostructure.

As expected, in Fig. 10, when material consuming is the same, the cluster-based structure has lower compliance than the structure composed of uniform microstructure. With regard to the disparate  $K$ , the red line in Fig. 10 is the relative percentage of compliance between the above two structures. From  $K = 2$  to 6, the stiffness promotion of cluster-based structure is from 22.67 to 54.82% compared with the uniform microstructure. However, the increasing magnitude is gradually slowing with increased  $K$ . When  $K = 2$  and 3, the stiffness promotion is from 22.67 to 37.34%, but when  $K = 5$  and 6, the stiffness promotion is only from 51.10 to 54.82%.

To further study the influence of microstructure distribution on structural stiffness, as illustrated in Fig. 11, a gradient structure composed of four microstructures is optimized. To guarantee the same material dosages with

Table 4 Comparisons between OC and HCA strategy

Optimization strategy	Time for 100 steps (s)	Discreteness (%)				
		Iteration	$M_p$	$M_{r1}$	$M_{r2}$	$M_{r3}$
OC	183.49	10	55.05	59.16	64.75	81.15
		22	19.67	44.70	10.59	18.01
		51	12.10	11.73	8.12	8.64
		100	12.19	12.02	10.43	7.77
HCA	137.91	10	2.16	2.97	2.60	5.35
		22	0.70	3.18	3.21	3.76
		51	2.27	1.37	2.01	2.62
		100	2.3	1.16	1.32	3.54

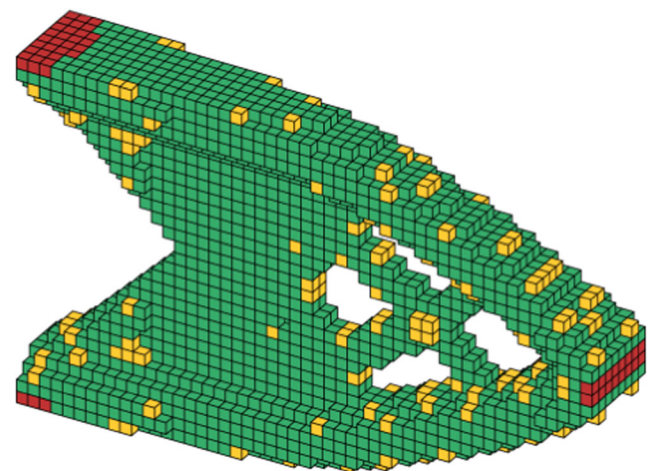
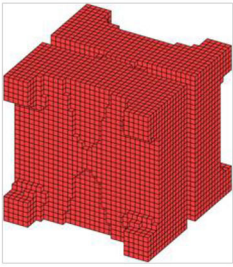
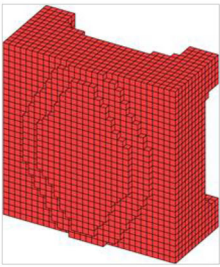
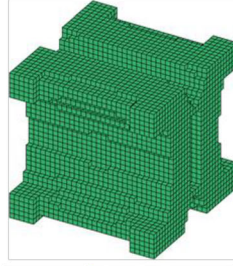
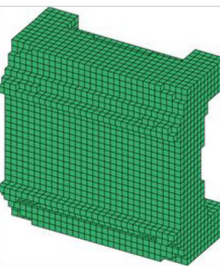
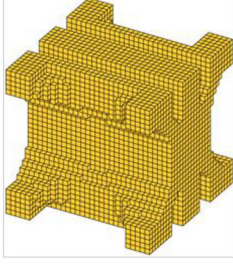
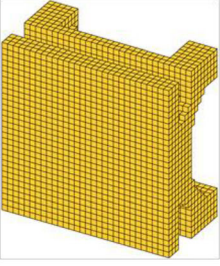


Fig. 15 The resulting topology of the macrostructure

**Table 5** The resulting microtopologies

Volume fraction (%)	Microstructure	Half of the microstructure
70		
55		
50		

clustering structure when  $K = 4$ , the volume fraction gradient varies from top to bottom as  $V_1^{\text{mic}} = 55.52\%$ ,  $V_2^{\text{mic}} = 37.02\%$ ,  $V_3^{\text{mic}} = 30.02\%$ , and  $V_4^{\text{mic}} = 25\%$ , respectively. Certainly, the gradient structure has worse stiffness performance ( $C = 569.49$ ) than the clustering structure ( $C = 341.68$ ). However, it is interesting to note that the stiffness of gradient structure is even worse than the structure composed of uniform microstructure ( $C = 497.63$ ). Such results demonstrate that due to the unreasonable material distributions, even with more microstructure forms, i.e., more design freedoms, the multi-material structure may still have a worse performance than the structure composed of uniform microstructure. From the above analysis, it is known that the clustering number and the material distribution locations are coupled to affect the resulting structural stiffness.

**Example 2** In this example, both the macro and microstructures are simultaneously optimized. The total numbers of microstructure are assumed as  $K = 3$ . The macro volume fractions are restrained as  $V^{\text{mac}} = 70\%$ ,  $50\%$ , and  $30\%$ ,

respectively. Corresponding to different  $V^{\text{mac}}$ , the microvolume fraction is uniformly designated as  $V_1^{\text{mic}} = 80\%$ ,  $V_2^{\text{mic}} = 57.5\%$ , and  $V_3^{\text{mic}} = 50\%$  with  $\zeta = 2$ , respectively.

For the comparison, the optimized results with uniform microstructure are also given in Fig. 12. Similar as the first example, the clustering structures have better stiffness performance than that composed of uniform microstructure. The material distributions reflect the load-transmission contributions of different parts in the macrostructure as well. With the decreasing of  $V^{\text{mac}}$ , the percentages of disparate microstructures are listed in Table 3. It is interesting that, accompanied with the variation of  $V^{\text{mac}}$ , the dosages of strong materials (microstructure 1 and 2) are increasing. This is because that when  $V^{\text{mac}}$  is small, materials are required to be more efficiently filled in the design domain such that strong materials are priority preferred.

As illustrated in Fig. 13, when  $V^{\text{mac}} = 30\%$ , the numerical procedure starting from the initial design to the converged results in Fig. 12 needs 51 iterations. It is noted that the topological configurations in Fig. 13 have no post-processing. The

expressions  $M_P = \sum_{m=1}^M 4P_m(1-P_m)/M \times 100\%$  and  $M_{rk} = \sum_{n=1}^N 4r_{kn}(1-r_{kn})/N \times 100\%$  (Sigmund 2007) are adopted to measure the discreteness of macro and microdesign variables. If a discrete design is obtained,  $M_P$  or  $M_{kn}$  becomes 0%, and if the design is full of intermediate value 0.5,  $M_P$  or  $M_{kn} = 100\%$ .

To show the advantages of the proposed method, Table 4 provides the comparisons between Optimality Criteria (OC) and HCA from the aspects of iterative time and discreteness of design variables based on a computer with 8 Intel Core i7-6700 processor, and 16GB memory. One may see that HCA is faster than OC within per 100 iterations. Moreover, the values of  $M_P$  and  $M_{kn}$  obtained by HCA are lower especially in the early iterations, indicating that the HCA may achieve a clear topology in much fewer iteration steps.

#### 4.1.1 3D example

Figure 14 presents a cantilever subjected to a distributed vertical load at the center of the right edge. The detailed geometric parameters are length  $L = 50$ , height  $H = 30$ , and width  $B = 8$ . The total types of microstructures are still assumed  $K = 3$ . The macro volume fraction is set as  $V^{\text{mac}} = 35\%$ . With  $\zeta = 2$ , microvolume fractions are respectively equal to  $V_1^{\text{mic}} = 70\%$ ,  $V_2^{\text{mic}} = 55\%$ , and  $V_3^{\text{mic}} = 50\%$ . The resulting compliance is  $C = 2927.62$ . The optimized macrostructure is presented in Fig. 15. Similar as the 2D case, the red microstructures are distributed around the regions where the force and constraints applied. The most design regions are occupied by the green microstructures. Only a few blue microstructures are attached to the green microstructures. The resulting microstructures are given in Table 5. This example illustrates the capability of the proposed model in 3D structures.

## 5 Conclusions

The clustering algorithm is introduced into HCA to achieve the topology optimization for heterogeneous structures in consideration of the locally non-uniformity on microscale. Through the quasi-static test and numerical results, the significant stiffness increase is observed of resulting structures compared with using uniform periodic cells. It is noted that the stiffness of the clustering structure can be continuously enhanced with increasing clustering number, but the magnitude increment is slowing. Besides, it is observed that even with more design freedoms, a poor material distribution may result in the nonperiodic structure worse performance than periodic structure. It is interesting to discover that with the macrovolume fraction decreasing, the dosages of strong materials are increasing.

Generally speaking, HCA is relatively much cheaper since the variable updating is heuristic-based, i.e., not using mathematical programming. Moreover, the proposed concurrent method based on HCA has advantages in iterative speed and capability of attaining clear topologies in fewer iterations. Without a sensitivity analysis, this method has certain potentials in solving crashworthiness and energy absorption topology optimization problems. However, this method has its shortcomings as well, e.g., suboptimal way of choosing volume fractions for microstructures, choosing proportional gain by trial and error, not being immediately extensible to multi-constrained problems.

**Funding information** This work was financially supported by the Natural Science Foundation of China (NSFC) (No. 11902015, 41804134), National Key Research and Development Program of China (2017YFB0103703), and the Fundamental Research Funds for the Central Universities, Beihang University, Young Elite Scientist Sponsorship Program by CAST.

## Compliance with ethical standards

**Conflict of interest** The authors declared that they do not have any commercial or associative interest that represents a conflict of interest in connection with the work submitted.

**Replication of results** All the results in this paper are generated by using MATLAB codes. The source codes can be available only for academic use from the corresponding author.

## References

- ASTM International A (2015) Standard test method for flexural properties of polymer matrix composite materials. ASTM International,
- Baughman RH, Zakhidov AA, de Heer WA (2002) Carbon nanotubes—the route toward applications. *Science* 297:787–792. <https://doi.org/10.1126/science.1060928>
- Coelho PG, Fernandes PR, Guedes JM, Rodrigues HC (2008) A hierarchical model for concurrent material and topology optimisation of three-dimensional structures. *Struct Multidiscip O* 35:107–115. <https://doi.org/10.1007/s00158-007-0141-3>
- Da DC (2019) Topology optimization design of heterogeneous materials and structures. Wiley, pp 29–55
- Da DC, Chen JH, Cui XY, Li GY (2017) Design of materials using hybrid cellular automata. *Struct Multidiscip O* 56:131–137. <https://doi.org/10.1007/s00158-017-1652-1>
- Deng JD, Yan J, Cheng GD (2013) Multi-objective concurrent topology optimization of thermoelastic structures composed of homogeneous porous material. *Struct Multidiscip O* 47:583–597. <https://doi.org/10.1007/s00158-012-0849-6>
- Evans AG, Hutchinson JW, Fleck NA, Ashby MF, Wadley HNG (2001) The topological design of multifunctional cellular metals. *Prog Mater Sci* 46:309–327. [https://doi.org/10.1016/S0079-6425\(00\)00016-5](https://doi.org/10.1016/S0079-6425(00)00016-5)
- Feyel F, Chaboche JL (2000) FE2 multiscale approach for modelling the elastoviscoplastic behaviour of long fibre SiC/Ti composite materials. *Comput Method Appl M* 183:309–330. [https://doi.org/10.1016/S0045-7825\(99\)00224-8](https://doi.org/10.1016/S0045-7825(99)00224-8)
- Gao LZ, Li H, Gao L (2019a) Topology optimization for multiscale design of porous composites with multi-domain microstructures. *Comput Method Appl M* 344:451–476. <https://doi.org/10.1016/j.cma.2018.10.017>

- Gao LZ, Li H, Li P, Gao L (2019b) Dynamic multiscale topology optimization for multi-regional micro-structured cellular composites. *Compos Struct* 211:401–417. <https://doi.org/10.1016/j.compstruct.2018.12.031>
- Jie G, Hao L, Liang G, Mi X (2018) Topological shape optimization of 3D micro-structured materials using energy-based homogenization method. *Adv Eng Softw* 116:89–102. <https://doi.org/10.1016/j.advengsoft.2017.12.002>
- Lakes R (1993) Materials with structural hierarchy. *Nature* 361:511–515. <https://doi.org/10.1038/361511a0>
- Li H, Luo Z, Gao L, Qin QH (2018) Topology optimization for concurrent design of structures with multi-patch microstructures by level sets. *Comput Method Appl M* 331:536–561. <https://doi.org/10.1016/j.cma.2017.11.033>
- Liang X, Du JB (2019) Concurrent multi-scale and multi-material topological optimization of vibro-acoustic structures. *Comput Method Appl M* 349:117–148. <https://doi.org/10.1016/j.cma.2019.02.010>
- Liu L, Yan J, Cheng GD (2008) Optimum structure with homogeneous optimum truss-like material. *Comput Struct* 86:1417–1425. <https://doi.org/10.1016/j.compstruc.2007.04.030>
- Niu B, Yan J, Cheng GD (2009) Optimum structure with homogeneous optimum cellular material for maximum fundamental frequency. *Struct Multidiscip O* 39:115–132. <https://doi.org/10.1007/s00158-008-0334-4>
- Patel NM, Kang BS, Renaud JE, Tovar A (2009) Crashworthiness design using topology optimization. *J Mech Design* 131 Artn:061013. <https://doi.org/10.1115/1.3116256>
- Rodrigues H, Guedes JM, Bendsoe MP (2002) Hierarchical optimization of material and structure. *Struct Multidiscip O* 24:1–10. <https://doi.org/10.1007/s00158-002-0209-z>
- Schaedler TA et al (2011) Ultralight metallic microlattices. *Science* 334:962–965. <https://doi.org/10.1126/science.1211649>
- Sigmund O (2007) Morphology-based black and white filters for topology optimization. *Struct Multidiscip O* 33:401–424. <https://doi.org/10.1007/s00158-006-0087-x>
- Sigmund O, Maute K (2013) Topology optimization approaches: a comparative review. *Struct Multidiscip O* 48:1031–1055. <https://doi.org/10.1007/s00158-013-0978-6>
- Sivapuram R, Dunning PD, Kim HA (2016) Simultaneous material and structural optimization by multiscale topology optimization. *Struct Multidiscip O* 54:1267–1281. <https://doi.org/10.1007/s00158-016-1519-x>
- Tan P-N, Steinbach M, Kumar V (2006) Introduction to data mining, 1st edn. Pearson Addison Wesley, Boston
- Tovar A, Patel NM, Niebur GL, Sen M, Renaud JE (2006) Topology optimization using a hybrid cellular automaton method with local control rules. *J Mech Des* 128:1205–1216. <https://doi.org/10.1115/1.2336251>
- Wang C, Zhu JH, Zhang WH, Li SY, Kong J (2018) Concurrent topology optimization design of structures and non-uniform parameterized lattice microstructures. *Struct Multidiscip O* 58:35–50. <https://doi.org/10.1007/s00158-018-2009-0>
- Wang QM, Jackson JA, Ge Q, Hopkins JB, Spadaccini CM, Fang NX (2016) Lightweight mechanical metamaterials with tunable negative thermal expansion. *Physical Review Letters* 117:175901. <https://doi.org/10.1103/PhysRevLett.117.175901>
- Xia L, Breitkopf P (2014) Concurrent topology optimization design of material and structure within FE2 nonlinear multiscale analysis framework. *Comput Method Appl M* 278:524–542. <https://doi.org/10.1016/j.cma.2014.05.022>
- Xia L, Breitkopf P (2015) Design of materials using topology optimization and energy-based homogenization approach in Matlab. *Struct Multidiscip O* 52:1229–1241. <https://doi.org/10.1007/s00158-015-1294-0>
- Xie YM, Zuo ZH, Huang XD, Rong JH (2012) Convergence of topological patterns of optimal periodic structures under multiple scales. *Struct Multidiscip O* 46:41–50. <https://doi.org/10.1007/s00158-011-0750-8>
- Xu B, Huang X, Zhou SW, Xie YM (2016) Concurrent topological design of composite thermoelastic macrostructure and microstructure with multi-phase material for maximum stiffness. *Compos Struct* 150:84–102. <https://doi.org/10.1016/j.compstruct.2016.04.038>
- Xu B, Xie YM (2015) Concurrent design of composite macrostructure and cellular microstructure under random excitations. *Compos Struct* 123:65–77. <https://doi.org/10.1016/j.compstruct.2014.10.037>
- Xu J et al (2018) Compressive properties of hollow lattice truss reinforced honeycombs (Honeytubes) by additive manufacturing: patterning and tube alignment effects. *Mater Design* 156:446–457. <https://doi.org/10.1016/j.matdes.2018.07.019>
- Xu J, Wu YB, Gao X, Wu HP, Nutt S, Yin S (2019) Design of composite lattice materials combined with fabrication approaches. *J Compos Mater* 53:393–404. <https://doi.org/10.1177/0021998318785710>
- Yan X, Huang X, Zha Y, Xie YM (2014) Concurrent topology optimization of structures and their composite microstructures. *Comput Struct* 133:103–110. <https://doi.org/10.1016/j.compstruc.2013.12.001>
- Yan XL, Huang XD, Sun GY, Xie YM (2015) Two-scale optimal design of structures with thermal insulation materials. *Compos Struct* 120:358–365. <https://doi.org/10.1016/j.compstruct.2014.10.013>
- Yao HB, Fang HY, Wang XH, Yu SH (2011) Hierarchical assembly of micro-/nano-building blocks: bio-inspired rigid structural functional materials. *Chem Soc Rev* 40:3764–3785. <https://doi.org/10.1039/c0cs00121j>
- Yin S, Li JN, Liu BH, Meng KP, Huan Y, Nutt SR, Xu J (2017) Honeytubes: hollow lattice truss reinforced honeycombs for crushing protection. *Compos Struct* 160:1147–1154. <https://doi.org/10.1016/j.compstruct.2016.11.007>
- Zhang W, Yin S, Yu TX, Xu J (2019) Crushing resistance and energy absorption of pomelo peel inspired hierarchical honeycomb. *Int J Impact Eng* 125:163–172. <https://doi.org/10.1016/j.ijimpeng.2018.11.014>
- Zhang WH, Sun SP (2006) Scale-related topology optimization of cellular materials and structures. *Int J Numer Methods Eng* 68:993–1011. <https://doi.org/10.1002/nme.1743>
- Zhang ZQ, Zhang YW, Gao HJ (2011) On optimal hierarchy of load-bearing biological materials. *Proceedings of the Royal Society B-Biological Sciences* 278:519–525. <https://doi.org/10.1098/rspb.2010.1093>
- Zhou SW, Li Q (2008) Design of graded two-phase microstructures for tailored elasticity gradients. *J Mater Sci* 43:5157–5167. <https://doi.org/10.1007/s10853-008-2722-y>

**Publisher's note** Springer Nature remains neutral with regard to jurisdictional claims in published maps and institutional affiliations.